

WiFo-M²: Plug-and-Play Multi-Modal Sensing via Foundation Model to Empower Wireless Communications

Haotian Zhang, *Graduate Student Member, IEEE*, Shijian Gao, *Member, IEEE*, Xiang Cheng, *Fellow, IEEE*

Abstract—The growing adoption of sensor-rich intelligent systems has boosted the use of multi-modal sensing to improve wireless communications. However, traditional methods require extensive manual design of data preprocessing, network architecture, and task-specific fine-tuning, which limits both development scalability and real-world deployment. To address this, we propose WiFo-M², a foundation model that can be easily plugged into existing deep learning-based transceivers for universal performance gains. To extract generalizable out-of-band (OOB) channel features from multi-modal sensing, we introduce ContraSoM, a contrastive pre-training strategy. Once pre-trained, WiFo-M² infers future OOB channel features from historical sensor data and strengthens feature robustness via modality-specific data augmentation. Experiments show that WiFo-M² improves performance across multiple transceiver designs and demonstrates strong generalization to unseen scenarios.

Index Terms—Foundation model, contrastive learning, diffusion, multi-modal sensing, transceiver design.

I. INTRODUCTION

The proliferation of multi-modal sensing, encompassing visual, Light Detection and Ranging (LiDAR), and other forms of environmental data, has become a cornerstone of emerging intelligent systems, from autonomous vehicles and smart factories to pervasive Internet of Things deployments [1]. Correspondingly, the wireless communications community is actively exploring how these ubiquitous sensing sources can be leveraged to optimize wireless communication performance. To systematically give the design principle and underlying mechanisms of sensing-aided communications, Cheng *et al.* proposed the first framework of this field, Synesthesia of Machines (SoM). To date, numerous studies have investigated promising applications, such as using multi-modal sensors to reduce pilot overhead for channel estimation [3], [4], employing images for beam selection [5]–[7], and exploiting on-vehicle sensors to aid multi-user precoding [8]–[10].

However, two fundamental challenges hinder the wider adoption and effectiveness of multi-modal sensing in communication systems. First, the prevailing design paradigm remains largely task-specific and scenario-bound. As shown in Fig. 1, Existing approaches typically rely on meticulously

Haotian Zhang and Xiang Cheng are with the State Key Laboratory of Photonics and Communications, School of Electronics, Peking University, Beijing 100871, P. R. China (e-mail: haotianzhang@stu.pku.edu.cn; xiangcheng@pku.edu.cn).

Shijian Gao is with the Internet of Things Thrust, The Hong Kong University of Science and Technology (Guangzhou), Guangzhou 511400, P. R. China (e-mail: shijiangao@hkust-gz.edu.cn).

customized data processing pipelines and network architectures tailored for narrow objectives, resulting in performance gains that lack universality and entail significant engineering overhead. Second, current research has concentrated primarily on a limited set of transceiver modules (e.g., beam prediction and handover) whose outputs are strongly correlated with visual object detection. The potential of leveraging sensing to enhance a wider range of core transceiver modules, such as channel interpolation and prediction, remains largely untapped due to the complex and often latent relationships between sensing data and various transceiver modules.

To overcome these limitations, a generic method is urgently needed to exploit multi-modal sensing for stable and universal performance gains without extra engineering efforts. This imperative naturally raises the question: *How can multi-modal sensing be transformed into task-agnostic feature representations that benefit diverse transceiver modules?* Inspired by the emerging paradigm of foundation models (FM) [11], [12], we aim to build one that extracts *universal, task-agnostic* features representing out-of-band (OOB) channel information. It would serve as a plug-and-play performance booster, adaptable to various transceiver modules.

To achieve this, we propose WiFo-M², the first universal foundation model for wireless communication performance enhancement, as shown in Fig. 1. To establish one-to-one positive sample pairs between CSI and multi-modal sensory data, we first develop a unified multi-modal sensing processing pipeline. Then, we design the ContraSoM pre-training strategy, which is designed to align the high-dimensional representations from WiFo-M² with their corresponding CSI features in the latent space. This alignment allows the WiFo-M² to extract universally beneficial supplementary features for diverse transceiver modules. To bridge the sampling rate gap, WiFo-M² is designed as a temporal sequence-to-sequence model. It ingests a fixed historical window of sensory data and is trained to extrapolate future CSI-aligned features. This enables WiFo-M² to provide supplementary CSI features even when fresh sensory data is temporarily unavailable, a practical issue largely overlooked in prior work. To enhance the robustness and representation learning capability of WiFo-M², ContraSoM incorporates modality-specific data augmentation techniques, including pixel-level transformations for images and diffusion-based feature-space augmentation specifically designed for the sparse and irregular structure of LiDAR point clouds. Our key contributions are summarized as follows:

- We develop WiFo-M², the first FM that can bring uni-

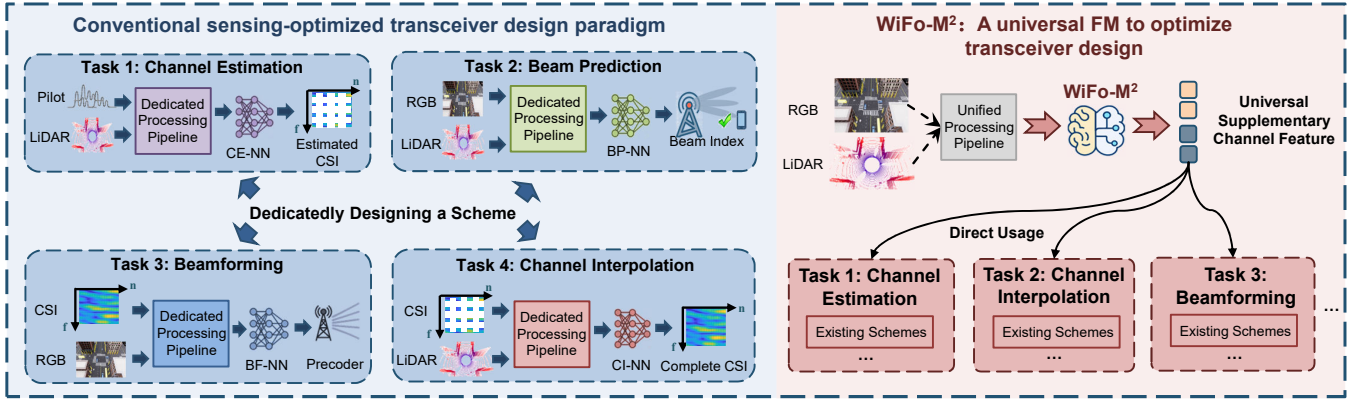


Fig. 1: Comparison between conventional sensing-optimized communications paradigm and the proposed WiFo-M² paradigm.

versal gains across diverse transceiver modules via multi-modal sensing. WiFo-M² offers a new paradigm for sensing-aided communications field, avoiding the cumbersome steps traditionally required. As such, WiFo-M² expands the set of transceiver modules that can be optimized through sensing, moving beyond the traditionally limited scope.

- We propose a pre-training strategy based on contrastive learning, named *ContraSoM*. By pre-training on a large-scale multi-modal dataset, the ContraSoM strategy endows WiFo-M² with the ability to mine universal OOB channel features during the inter-frame perception gap.
- We apply WiFo-M² to a wide range of existing transceiver design schemes. Experimental results demonstrate that the proposed WiFo-M² can provide universal performance gains without requiring fine-tuning and exhibits strong cross-scenario generalization capabilities.

II. RELATED WORK

A. Sensing-Assisted Wireless Communications

Multi-modal sensing has been increasingly utilized to improve wireless communication performance. Existing schemes are predominantly task-specific, requiring carefully customized data processing and network designs for each application. For example, the LE-CLN scheme [3] converts raw LiDAR data into the signal propagation feature superposed range map and customizes a feature extraction neural network (NN) to transform LiDAR into OOB features beneficial for channel estimation. Similarly, the H-MVMM scheme proposed in [8] is specifically designed for precoding, with carefully crafted data processing methods for Global Positioning System (GPS), LiDAR, and RGB images, as well as customized feature extraction and fusion NNs. The radar-based channel estimation method proposed in [4] extracts propagation delay, velocity, and angle parameters from radar data via clutter removal, 3D-FFT, and peak detection to guide sparse channel estimation. Such design principle leads to a fundamental limitation: the performance gain lacks universality and is only effective for a particular task, dataset, and transceiver setup.

Another pressing issue is that current research remains concentrated on just a few transceiver modules whose outputs are strongly tied to user location, such as beam prediction and

handover. To date, whether multi-modal sensing can benefit many other transceiver modules is still largely unexplored. The difficulty stems from the highly diverse and often latent relationships between sensing and transceiver modules. For example, temporal channel prediction (CP) relies on capturing the time-varying characteristics of scatterers; uplink–downlink CP concerns spatial consistency across frequency bands. Hence, crafting an dedicated sensing pipeline and mining task-specific features becomes labor-intensive. In this context, obtaining a universal beneficial feature from multi-modal sensing becomes an attractive topic. This study is the first to demonstrate that multi-modal sensing can boost channel interpolation and channel prediction via WiFo-M², two core transceiver modules that had not been explored for such benefits until now.

B. Contrastive Learning for Cross-Modal Alignment

As a powerful self-supervised paradigm, CL has emerged as a foundational technique for aligning heterogeneous data modalities by learning a shared semantic space. Beyond vision-language domains, CL has been effectively adapted to align sensor modalities with complementary characteristics. Extending this idea, DiffCL [14] introduces a diffusion-based graph CL module that generates denoised visual- and text-aware views, encouraging the encoder to distil robust user–item representations even under severe interaction sparsity and multimodal noise. In medical image segmentation, CLMorph [15] integrates CL into a deformable registration framework to align an unaligned image with a reference image. By contrasting feature representations extracted from these images, it enhances the discriminative capacity of the network. In industrial time-series generation, MetaIndux-TS [16] employs a contrastive synthesis layer within its diffusion framework to enhance generation fidelity. This layer explicitly compares the synthesized sequences with the original noisy input, guiding the model to better capture fine-grained deviations and improve the overall quality of generated data.

Building upon these advances, CL has also been introduced as an effective pre-training strategy in wireless communication community. For instance, CSI-CLIP proposed in [17] treats channel state information (CSI) and channel impulse response as naturally aligned pairs and performs cross-modal CL between them, enabling the model to capture generalizable

channel features for improved positioning and beam management. LWLM [18] introduces Position-Invariant CL, which contrasts CSI samples collected from the same location under different base station (BS) configurations to learn robust and location-aware semantics specifically for localization tasks. Furthermore, in [19], a VLM-based beam prediction (BP) framework is proposed which utilizes CL to align image and LiDAR features, enforcing cross-modal consistency to enhance multi-modal fusion for beam selection. Most recently, the WMFM model [20] adopts a vanilla form of CL to align images with CSI, yet it still suffers from several limitations. Firstly, as in most prior work, it fails to resolve the intrinsic temporal mismatch between sensory data and CSI. Secondly, it utilizes solely the image modality and does not employ any data pre-processing and augmentation techniques, limiting its robustness and cross-domain generalization. Thirdly, the pre-training dataset covers only one scene and a single communication system configuration. Finally, it does not investigate how multi-modal sensing could benefit a wider range of transceiver modules and remains confined to Line of sight (LoS)/non-Line of sight (NLoS) classification and localization.

III. SYSTEM MODEL, PROBLEM DESCRIPTION, AND CHALLENGES

A. System Model and Problem Description

We consider a typical intelligent system scenario in B5G/6G, e.g., an intelligent transportation system, where BS is equipped with multi-modal sensors for environmental monitoring and situational awareness. In this work, we assume that multi-modal sensing includes LiDAR point clouds and RGB images, denoted by $P_{\text{raw}} \in \mathbb{R}^{N \times 3}$ and $I \in \mathbb{R}^{3 \times H \times W}$, respectively. We consider a multiple-input single-output orthogonal frequency division multiplexing (MISO-OFDM) communication system where BS is equipped with either a uniform linear array (ULA) or a uniform planar array (UPA), with the antenna size denoted by N and the number of subcarriers by K . The BS serves M single-antenna users. Let $\mathbf{H} \in \mathbb{C}^{K \times N}$ represent CSI between the BS and a certain user.

In wireless communication systems, to establish a reliable link, the BS and users must go through a series of predefined steps, including but not limited to pilot transmission, channel estimation, full-band interpolation, precoder/decoder design, CP for high-mobility cases, and data detection. Each of these steps collectively constitutes the transceiver-design pipeline. The problem addressed in this paper is how to leverage multi-modal sensing as external OOB information to assist various stages of the transceiver design, with the ultimate goal of streamlining and optimizing transceiver design to build a higher-performance communication system.

B. Challenges

WiFo-M² aims to serve as an FM capable of extracting universal OOB channel features from multi-modal sensing. Achieving this requires a self-supervised pre-training scheme that (i) learns from large-scale unlabeled data and (ii) aligns heterogeneous modalities. CL [13], which constructs representations by learning similarities between data samples, naturally meets the above requirements. CL [13] satisfies these criteria,

yet its vanilla form is inadequate for WiFo-M². Substantial modifications are needed in both the pre-training strategy and the model architecture to cope with the unique challenges posed by multi-modal sensing and wireless channels. The key obstacles are:

(1) *Absence of Inherent Cross-Modal Data Pairing:* A fundamental premise for CL is the availability of aligned positive sample pairs across modalities. In wireless communication scenarios, however, a single sensing frame captures elements like vehicles and buildings can correspond to multiple potential receivers. Consequently, the first challenge lies in disentangling and constructing matching CSI positive pairs for different receivers from the same set of sensory data.

(2) *Temporal Misalignment Due to Heterogeneous Sampling Rates:* The goal of sensing-aided communications is to provide OOB channel feature at the same measurement rate as the CSI estimation itself. However, a fundamental gap exists: CSI refreshes every few milliseconds, but cameras and LiDAR operate at low frame rates (e.g., 10-20 Hz). Most channel samples thus lack a concurrent sensing frame. Therefore, the model cannot rely on simply aligning sensory frames with coincident CSI samples. Instead, it has to effectively “fill in” the missing environmental context at the communication system’s operational tempo.

(3) *Difficulty in Designing Effective Multi-modal Data Augmentation:* Data augmentation is crucial for generating diverse, semantic-preserving views to learn robust representations. However, crafting augmentation strategies for complex, unstructured modalities like LiDAR point clouds is non-trivial. Simple operations like random point dropout or perturbation can easily corrupt geometric relationships, undermining both the authenticity of the simulation and the consistency required for CL. Effective augmentation method should be developed to maintain the data’s fundamental spatial and semantic structure to ensure the generated views remain valid positive samples.

IV. WiFo-M² FRAMEWORK: SENSING PROCESSING, FEATURE EXTRACTION, AND PRE-TRAINING

In this section, we introduce the core designs of WiFo-M²: a unified sensing processing pipeline that addresses Challenge 1, the model architecture and feature extraction method that tackles Challenge 2, and a dedicated pre-training strategy for WiFo-M² that equips WiFo-M² with essential capabilities while effectively resolving Challenge 3. The overall framework of WiFo-M² is depicted in Fig. 2.

A. Unified Sensing Processing Pipeline of WiFo-M²

1) *Image Processing Pipeline:* The image processing pipeline converts raw images containing many potential receivers into a representation deterministically linked to the CSI of a specific transmitter and receiver pair, and it comprises three core steps.

Step 1: Initial Object Detection and Tracking. The raw image data is first subjected to a pixel-level augmentation pipeline (described in detail in Section IV-C1), and the resulting image is denoted as \tilde{I} . The image processing pipeline begins with object detection to identify potential

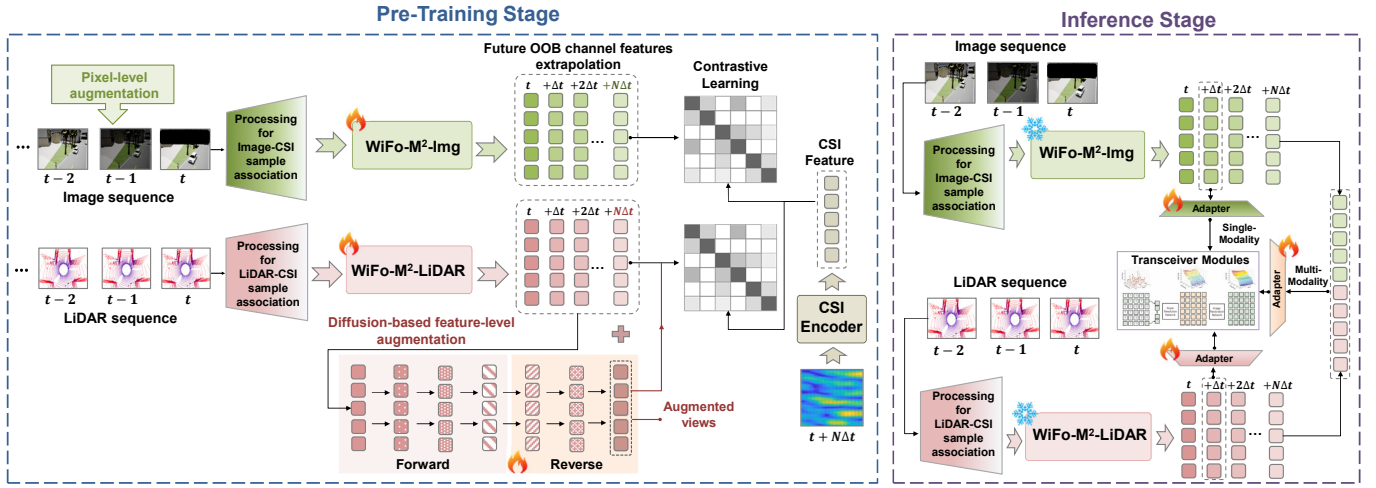


Fig. 2: Overall framework of WiFo-M², illustrating the two-stage pipeline: (left) pre-training using ContraSoM strategy, and (right) inference stage for optimizing transceiver design.

communication targets (e.g., vehicles in V2X communication scenarios) from $\tilde{\mathcal{I}}$. We assume the BS has prior knowledge of the receiver's initial position through initial access procedures. Then, the advanced object detection model YOLOv8 [24] is used to detect all targets in the image and perform continuous tracking across frames.

Step 2: Receiver-Bounding Box Matching. For each detected bounding box, we calculate its angular span in the camera's field of view. Given a bounding box with normalized coordinates (x_c^n, y_c^n, w^n, h^n) where x_c^n, y_c^n are the normalized center coordinates and w^n, h^n are the normalized width and height, we first convert to pixel coordinates: $x_c = x_c^n \times W$, $y_c = y_c^n \times H$, $w = w^n \times W$, and $h = h^n \times H$, where W and H are the image width and height in pixels. The horizontal angular span $[\theta_{\min}, \theta_{\max}]$ of the bounding box is then computed using the camera's intrinsic parameters:

$$\theta_{\min} = \arctan \left(\frac{x_{\min} - c_x}{f_x} \right), \quad (1)$$

$$\theta_{\max} = \arctan \left(\frac{x_{\max} - c_x}{f_x} \right), \quad (2)$$

where $x_{\min} = x_c - w/2$, $x_{\max} = x_c + w/2$, f_x is the focal length in pixels, and c_x is the principal point offset along the x-axis.

To match the receiver with the correct bounding box, we compute the receiver's azimuth angle relative to camera. Given the camera's world coordinates $\mathbf{p}_{\text{cam}} = (x_{\text{cam}}, y_{\text{cam}}, z_{\text{cam}})$ and yaw angle ψ_{cam} , and the receiver's world coordinates $\mathbf{p}_{\text{rec}} = (x_{\text{rec}}, y_{\text{rec}}, z_{\text{rec}})$, the relative azimuth angle is:

$$\theta_{\text{rec}} = \text{wrap} \left(\arctan \left(\frac{y_{\text{rec}} - y_{\text{cam}}}{x_{\text{rec}} - x_{\text{cam}}} \right) - \psi_{\text{cam}} \right), \quad (3)$$

where $\text{wrap}(\cdot)$ ensures the angle remains within $(-\pi, \pi]$. The bounding box whose angular span contains θ_{rec} is selected as the match. If multiple bounding boxes satisfy this condition, we choose the one whose angular center $\bar{\theta} = (\theta_{\min} + \theta_{\max})/2$ is closest to θ_{rec} .

Step 3: Receiver-Labeling via Angular Encoding. Once the matching bounding box is identified, we perform a

receiver-labeling operation by replacing the original pixel content within the bounding box with a color that encodes the receiver's angular information. Through this operation, a positive sample association between the processed image and the CSI between BS and a specific user is established, and geometric information is also directly embedded into the image for subsequent feature learning.

The angular encoding proceeds as follows. First, we clip the receiver's azimuth angle to the range $[-\pi/2, \pi/2]$, i.e., $\theta_{\text{clipped}} = \max(-\frac{\pi}{2}, \min(\frac{\pi}{2}, \theta_{\text{rec}}))$. Next, we normalize this angle to the range $[0, 1]$ by $\theta_{\text{norm}} = (\theta_{\text{clipped}} + \pi/2)/\pi$. Finally, we map the normalized angle to a hue value in the HSV color space via $h = \lfloor 179 \times \theta_{\text{norm}} \rfloor$. The corresponding RGB color $\mathbf{c}_{\text{RGB}} = (r, g, b)$ is obtained by converting the HSV color $(h, 255, 255)$ to the RGB color space. The bounding box region is then filled with this color:

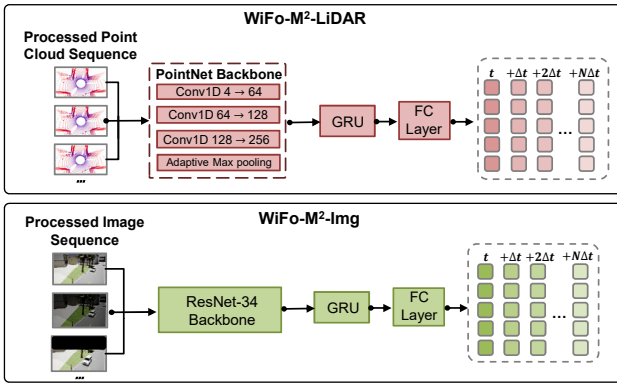
$$\tilde{\mathbf{I}}(y_1 : y_2, x_1 : x_2) = \mathbf{c}_{\text{RGB}}, \quad (4)$$

where (x_1, y_1) and (x_2, y_2) define the bounding box corners in pixel coordinates. The transformed image after this operation is denoted as $\mathbf{I}_{\text{labeled}}$.

2) LiDAR Processing Pipeline: Given a raw point cloud $\mathbf{P}_{\text{raw}} \in \mathbb{R}^{N \times 3}$ consisting of N points with 3D coordinates (x, y, z) , we first remove ground points and obtain a filtered point cloud $\mathbf{P}_{\text{filt}} \in \mathbb{R}^{N' \times 3}$.

Step 1: Object Clustering and Initial Receiver Matching. To segment the filtered point cloud into distinct objects, we apply the DBSCAN clustering algorithm to \mathbf{P}_{filt} , obtaining a set of clusters $\mathcal{C} = \{C_1, C_2, \dots, C_K\}$. For each cluster C_k , we compute its centroid $\mathbf{c}_k = (x_k, y_k, z_k)$. During the initial access phase, the receiver reports its global position $\mathbf{p}_{\text{rec}} = (x_{\text{rec}}, y_{\text{rec}}, z_{\text{rec}})$. The receiver-corresponding cluster is identified as the one whose centroid is closest to \mathbf{p}_{rec} : $k^* = \arg \min_k \|\mathbf{c}_k - \mathbf{p}_{\text{rec}}\|$.

Step 2: Continuous Tracking and Point Labeling. Once the receiver cluster is identified in the initial frame, we employ a multi-object tracking algorithm to maintain consistent cluster identities across consecutive frames. This ensures that the receiver vehicle is correctly associated throughout the

Fig. 3: Network architecture of WiFo-M²-Img/LiDAR.

sequence. Let the receiver cluster be denoted as \mathcal{C}_{rec} , and let the set of building points be defined by a geometric rule, e.g., $\mathcal{B} = \{p_i \in \mathbf{P}_{\text{filt}} : y_i > y_{\text{build}}\}$. Then each point $p_i = (x_i, y_i, z_i)$ in \mathbf{P}_{filt} is assigned a label $l_i \in \{-1, 0, 1\}$ according to:

$$l_i = \begin{cases} 1, & \text{if } p_i \in \mathcal{C}_{\text{rec}} \\ -1, & \text{if } p_i \in \mathcal{B} \setminus \mathcal{C}_{\text{rec}} \\ 0, & \text{otherwise} \end{cases} \quad (5)$$

Finally, the labeled point cloud $\mathbf{P}_{\text{labeled}} \in \mathbb{R}^{N' \times 4}$ is then constructed by appending the label column to \mathbf{P}_{filt} , i.e., $\mathbf{P}_{\text{labeled}} = [\mathbf{P}_{\text{filt}}, \mathbf{l}]$, where $\mathbf{l} = [l_1, l_2, \dots, l_{N'}]^T$.

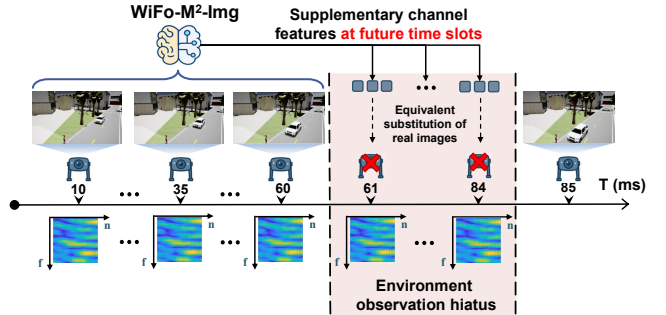
B. Network Architecture and Working Flow of WiFo-M²

The WiFo-M² consists of two modality-specific backbones: WiFo-M²-Img built upon ResNet-34 [22], and WiFo-M²-LiDAR built upon PointNet [23]. Essentially, these two backbones act as modality-specific feature extractors. Their architectures are depicted in Fig. 3. To capture temporal dependencies in sequential sensing data, WiFo-M²-Img and WiFo-M²-LiDAR are augmented with Gated Recurrent Units (GRU) for sequential processing.

1) *CSI Feature Extraction*: For CSI feature extraction, we employ the pre-trained WiFo model [21] as a powerful spatio-temporal-frequency (STF) feature extractor. Given an input CSI data $\mathbf{H} \in \mathbb{C}^{K \times N}$, the WiFo model processes it through its transformer-based encoder. The output is a fixed-dimensional feature vector $\mathbf{z}^C \in \mathbb{R}^d$.

2) *Image and LiDAR Feature Extraction*: Both image and LiDAR modalities follow the same feature extraction procedure comprising three stages:

Stage 1: Spatial Feature Extraction. Let T denote the timestamp of the most recent sensory data. Define Δt_I and Δt_L as the inter-frame intervals of the image and LiDAR streams, respectively, and (n_I+1) and (n_L+1) as the sequence lengths of the LiDAR and image inputs. For image modality, each frame $\mathbf{I}_{\text{labeled}}^t$ passes through the ResNet-34 backbone of the WiFo-M²-Img model to obtain frame-level features. For LiDAR modality, each point cloud frame $\mathbf{P}_{\text{labeled}}^t$ is processed

Fig. 4: Temporal feature extrapolation in WiFo-M²-Img.

by the PointNet backbone [23] to extract frame-level features. The extraction process can be formally expressed as:

$$\mathbf{u}_t^I = f_{\text{ResNet}}(\mathbf{I}_{\text{labeled}}^t) \in \mathbb{R}^d, \quad t = T - n_I \Delta t_I, \dots, T \quad (6)$$

$$\mathbf{u}_t^L = f_{\text{PointNet}}(\mathbf{P}_{\text{labeled}}^t) \in \mathbb{R}^d, \quad t = T - n_L \Delta t_L, \dots, T \quad (7)$$

where f_{ResNet} and f_{PointNet} denote the ResNet and PointNet backbone networks respectively. We denote the frame-level features for image and LiDAR within a time window $[T - n_I \Delta t_I, T]$ or $[T - n_L \Delta t_L, T]$ as $\mathbf{u}_t^I \in \mathbb{R}^d$ and $\mathbf{u}_t^L \in \mathbb{R}^d$, respectively.

Stage 2: Temporal Feature Modeling. To capture temporal dependencies, both modalities employ the GRU network that learns the underlying dynamics of the environment. The GRU processes the sequences of intermediate frame-level features $\{\mathbf{u}_t^x\}_{t=T-n_x \Delta t_x}^T$, $x \in \{L, I\}$ to produce a sequence of hidden states, which are then projected to the final feature space. Let $\Delta \tau$ be the CSI estimation interval. The resulting projected feature sequence corresponds to the prediction window $[T, T + \Delta \tau, \dots, T + \Delta t_x]$, i.e., from the current sensing timestamp T up to the moment when the next sensing frame is captured. This operation can be expressed as:

$$\mathbf{v}_\tau^x = \phi_x \left(\mathcal{G}_x \left(\{\mathbf{u}_t^x\}_{t=T-n_x \Delta t_x}^T \right) \right), \quad \tau = T, \dots, T + \Delta t_x \quad (8)$$

where \mathcal{G}_x denotes the GRU network for modality x , ϕ_x represents the projection layer, and $\mathbf{v}_t^x \in \mathbb{R}^d$ is the final frame-level feature at time step t for modality x . The sequence of final features $\{\mathbf{v}_\tau^x\}_{\tau=T}^{T+\Delta t_x}$ is then used for subsequent temporal alignment and contrastive learning.

Stage 3: Multi-Timestamp Feature Generation and Alignment. A key design of WiFo-M²'s architecture is that the GRU generates features for multiple future timestamps simultaneously. During pre-training, the sequence of final features $\{\mathbf{v}_\tau^x\}_{\tau=T}^{T+\Delta t_x}$, $x \in \{L, I\}$ generated by WiFo-M² are individually aligned with the CSI feature at the corresponding timestamp. For a given timestamp τ , a certain sensing feature \mathbf{v}_τ^x is selected and paired with the CSI feature \mathbf{z}_τ^C from the same timestamp to form a positive pair for CL (detailed in the next section). As shown in Fig. 4, this design enables WiFo-M² to learn to generate temporally aligned features at specific future timestamps, which can then be directly compared with CSI features from the corresponding time in the CL objective, ensuring precise cross-modal temporal alignment.

C. Pre-training Strategy for WiFo-M²: ContraSoM

This section presents the proposed ContraSoM pre-training strategy in detail, covering the modality-specific data-augmentation techniques together with the overall contrastive learning pipeline. By aligning multi-modal sensing and wireless channel in the latent space, ContraSoM essentially performs the SoM processing outlined in [2].

1) *Modality-Specific Data Augmentation*: Image data possess a regular grid structure and dense pixel representation, making them amenable to direct augmentation in the pixel space. We apply a series of stochastic transformations to generate robust augmented views for contrastive learning. Given an input image \mathbf{I} , the augmented view $\tilde{\mathbf{I}}$ is obtained via: $\tilde{\mathbf{I}} = \mathcal{T}_{\text{aug}}(\mathbf{I})$. \mathcal{T}_{aug} is a combination of several of the following operations, randomly applied to each original image: First, color jitter randomly perturbs brightness, contrast, saturation, and hue, mimicking natural variations in illumination: $\mathbf{I}_{\text{jit}} = \mathbf{I} \odot \mathbf{c}_{\text{scale}} + \mathbf{c}_{\text{shift}}$, where \odot denotes element-wise multiplication, $\mathbf{c}_{\text{scale}} \sim \mathcal{U}(0.7, 1.3)$ and $\mathbf{c}_{\text{shift}} \sim \mathcal{U}(-0.3, 0.3)$ for each channel. Second, Gaussian Blur is applied with probability $p = 0.5$ to simulate lens defocus or motion blur: $\mathbf{I}_{\text{blur}} = \mathbf{I} * G_{\sigma}$ with $\sigma \sim \mathcal{U}(0.1, 2.0)$, where $*$ denotes the convolution operation and G_{σ} is a Gaussian kernel of size 15×15 . Next, random erasing is performed with probability $p = 0.3$, which randomly selects a rectangular region \mathcal{R} within the image and replaces the pixel values in that region with random noise, emulating occlusions or sensor dropout. This operation is defined as:

$$\mathbf{I}_{\text{erase}}(x, y) = \begin{cases} \eta, & \text{if } (x, y) \in \mathcal{R} \\ \mathbf{I}(x, y), & \text{otherwise} \end{cases}, \quad (9)$$

where $\eta \sim \mathcal{U}(0, 1)$, and the region \mathcal{R} has an area ratio $\sim \mathcal{U}(0.01, 0.05)$ and an aspect ratio $\sim \mathcal{U}(0.3, 3.3)$. Finally, normalization is applied using ImageNet statistics: $\mathbf{I}_{\text{norm}} = (\mathbf{I} - \boldsymbol{\mu})/\boldsymbol{\sigma}$ with $\boldsymbol{\mu} = [0.485, 0.456, 0.406]$ and $\boldsymbol{\sigma} = [0.229, 0.224, 0.225]$. This pipeline encourages the model to learn invariant representations under appearance variations, occlusion, and noise.

LiDAR point clouds are sparse and geometrically structured. Applying noise directly in the raw data level would easily disrupt semantic relationships. Therefore, we propose to perform augmentation in the feature space. We adopt a denoising diffusion probabilistic model (DDPM) framework to generate augmented features in a controlled manner.

The augmentation process begins with a forward noising step. Taking the final LiDAR feature at a specific time step i , denoted as \mathbf{v}_i^L , as an example, we gradually inject Gaussian noise into this original feature over a series of M discrete steps. This forward noising process is defined as a Markov chain:

$$q(\mathbf{v}_m \mid \mathbf{v}_{m-1}^L) = \mathcal{N}\left(\mathbf{v}_m^L; \sqrt{1 - \beta_m} \mathbf{v}_{m-1}^L, \beta_m \mathbf{I}\right), \quad (10)$$

where β_m follows a linearly increasing schedule from $\beta_{\min} = 5 \times 10^{-6}$ to $\beta_{\max} = 2 \times 10^{-3}$, $m = 1, \dots, M$. Due to the additive property of Gaussian noise, we can directly sample the feature at any step m :

$$\mathbf{v}_m^L = \sqrt{\alpha_m} \mathbf{v}_i^L + \sqrt{1 - \alpha_m} \boldsymbol{\epsilon}, \quad \boldsymbol{\epsilon} \sim \mathcal{N}(0, \mathbf{I}) \quad (11)$$

with $\alpha_m = 1 - \beta_m$ and $\bar{\alpha}_m = \prod_{s=1}^m \alpha_s$.

For efficient feature generation, we employ the Denoising Diffusion Implicit Models (DDIM) sampling during the reverse process, where the noise predictor $\epsilon_{\theta}(\cdot)$ is a learnable NN. Starting from a randomly sampled noisy feature \mathbf{v}_m^L , the DDIM sampler with stride $\Delta m = \max([m/u], 1)$ (where $u = 8$) efficiently recovers a cleaned feature in fewer steps:

$$\begin{aligned} \mathbf{v}_{m-\Delta m}^L &= \sqrt{\bar{\alpha}_{m-\Delta m}} \left(\frac{\mathbf{v}_m^L - \sqrt{1 - \bar{\alpha}_m} \epsilon_{\theta}(\mathbf{v}_m^L, m)}{\sqrt{\bar{\alpha}_m}} \right) \\ &+ \sqrt{1 - \bar{\alpha}_{m-\Delta m}} \epsilon_{\theta}(\mathbf{v}_m^L, m). \end{aligned} \quad (12)$$

After $U = 24$ reverse steps, we obtain the augmented feature $\tilde{\mathbf{v}}_i^L$. To enhance diversity, we generate two distinct augmented views $\tilde{\mathbf{v}}_i^L(1)$ and $\tilde{\mathbf{v}}_i^L(2)$ by starting from different noise samples:

$$\tilde{\mathbf{v}}_i^L(1) = \text{DDIM}(\mathbf{v}_i^L, \epsilon_1, m_1), \quad \tilde{\mathbf{v}}_i^L(2) = \text{DDIM}(\mathbf{v}_i^L, \epsilon_2, m_2),$$

where $m_1, m_2 \sim \mathcal{U}\{200, 400\}$ represent the initial diffusion steps, and $\epsilon_1, \epsilon_2 \sim \mathcal{N}(0, \mathbf{I})$ are two independent Gaussian noise vectors. The two independent pairs (m_1, ϵ_1) and (m_2, ϵ_2) produce two distinct noised versions of the original feature, which act as separate deterministic starting points for the DDIM reverse process and ultimately yield the two complementary augmented views.

2) *Contrastive Learning Objectives in WiFo-M²*: We design two distinct CL frameworks for image-CSI alignment in WiFo-M²-Img and for LiDAR-CSI alignment in WiFo-M²-LiDAR.

For WiFo-M²-Img, we employ a symmetric contrastive learning objective between the extracted image feature \mathbf{v}^I and the CSI feature \mathbf{z}^C . To ensure balanced alignment between the two modalities, we define a symmetric InfoNCE loss:

$$\mathcal{L}^I = \mathcal{L}_{\text{sym}}(\mathbf{v}^I, \mathbf{z}^C), \quad (13)$$

where the symmetric InfoNCE loss for two feature sets \mathbf{Z}_a and \mathbf{Z}_b is:

$$\mathcal{L}_{\text{sym}}(\mathbf{Z}_a, \mathbf{Z}_b) = \frac{1}{2} [\mathcal{L}_{\text{InfoN}}(\mathbf{Z}_a, \mathbf{Z}_b) + \mathcal{L}_{\text{InfoN}}(\mathbf{Z}_b, \mathbf{Z}_a)]. \quad (14)$$

The standard InfoNCE loss for a batch of N feature pairs is defined as:

$$\mathcal{L}_{\text{InfoN}}(\mathbf{Z}_a, \mathbf{Z}_b) = -\frac{1}{N} \sum_{i=1}^N \log \frac{\exp(s(\mathbf{z}_a^{(i)}, \mathbf{z}_b^{(i)}) / \tau_e)}{\sum_{j=1}^N \exp(s(\mathbf{z}_a^{(i)}, \mathbf{z}_b^{(j)}) / \tau_e)}, \quad (15)$$

where $\mathbf{z}_a^{(i)}$ and $\mathbf{z}_b^{(i)}$ form a positive pair, $s(\cdot, \cdot)$ denotes the cosine similarity function, and τ_e is a temperature hyper-parameter. The symmetric formulation ensures bidirectional alignment between image and CSI feature spaces.

For the LiDAR modality, we incorporate both the original LiDAR feature \mathbf{v}^L and the two diffusion-augmented features $\tilde{\mathbf{v}}^L(1)$, $\tilde{\mathbf{v}}^L(2)$ into the contrastive learning framework. The overall objective consists of two components: a contrastive loss $\mathcal{L}_{\text{contra}}^L$ and a diffusion training loss $\mathcal{L}_{\text{diff}}$. Specifically, we formulate a triplet contrastive loss to enforce consistency between three pairs: the original LiDAR features and CSI features, and the augmented LiDAR features and CSI features:

$$\begin{aligned} \mathcal{L}_{\text{contra}} &= \lambda_1 \cdot \mathcal{L}_{\text{sym}}(\mathbf{v}^L, \mathbf{z}^C) + \lambda_2 \cdot \mathcal{L}_{\text{sym}}(\tilde{\mathbf{v}}^L(1), \mathbf{z}^C) \\ &+ \lambda_3 \cdot \mathcal{L}_{\text{sym}}(\tilde{\mathbf{v}}^L(2), \mathbf{z}^C). \end{aligned} \quad (16)$$

TABLE I: Overview of Pre-training Datasets.

Dataset Type	Data Source	Scenario	Carrier Frequency (GHz)	Dataset ID	BS Antenna Configuration	Bandwidth (GHz)	Number of Subcarriers	Samples
Pre-training Dataset	M ³ SC [27]	Intersection Traffic	28	I1	32 × 1	0.2	512	881
				I2	64 × 1	1	1024	868
				I3	16 × 8	0.8	512	886
				I4	16 × 8	0.4	512	896
				I5	8 × 8	0.8	1024	878
				I6	8 × 4	1	256	871
	SynthSoM [28]	Dense Building	4.95	B1	16 × 16	0.05	256	2270
				B2	16 × 8	0.05	512	2098
				B3	8 × 8	0.05	512	1852
				B4	8 × 4	0.1	512	2353
				B5	4 × 4	0.1	1024	2379

TABLE II: Overview of Testing Datasets.

Dataset Type	Data Source	Scenario	Carrier Frequency (GHz)	Dataset ID	BS Antenna Configuration	Bandwidth (GHz)	Number of Subcarriers	Samples
Testing Set (Seen Scenarios)	SynthSoM [28] M ³ SC [27]	Intersection Traffic & Dense Building	28, 4.95	L1	16 × 8	0.8 0.05	512	809
				L2	4 × 4	0.1	1024	547
				L3	16 × 16	0.05	256	300
				L4	8 × 4	1	256	229
				L5	32 × 1 8 × 4	0.2 0.1	512	725
				L6	64 × 1 8 × 8	1 0.8	64	404
				L7	8 × 8	0.05	512	437
	SynthSoM-Twin [30]	Campus	5.9	C1	64 × 1	0.02	64	480
		DeepSense-6G [32] (Measured data)	60	S1	16 × 1	—	—	387
		ViWi [31]	60	V1	64 × 1	0.5	256	1302

In parallel to the above contrastive objective, we incorporate a diffusion training loss to optimize the sampler $\epsilon_\theta(\cdot)$. This component follows the standard DDPM objective, minimizing the mean-squared error between the predicted and actual noise:

$$\mathcal{L}_{\text{diff}} = \mathbb{E}_{t, \mathbf{z}_0, \epsilon} [\|\epsilon - \epsilon_\theta(\mathbf{z}_t, t)\|^2], \quad (17)$$

with $t \sim \mathcal{U}\{1, \dots, T\}$ and $\epsilon \sim \mathcal{N}(0, \mathbf{I})$.

The complete training objective for WiFo-M²-LiDAR thus combines both losses with a balancing weight:

$$\mathcal{L}^{\mathbf{L}} = \mathcal{L}_{\text{contra}} + \lambda_{\text{diff}} \cdot \mathcal{L}_{\text{diff}}, \quad (18)$$

where $\lambda_{\text{diff}} = 0.3$ in our implementation.

V. EXPERIMENTS

In this section, we begin by detailing the construction of the pre-training and testing datasets. Next, we provide a detailed description of the network architecture and training hyperparameters. Finally, we comprehensively evaluate and analyze the performance of WiFo-M².

A. Datasets

We construct a multi-modal pre-training dataset that includes LiDAR, RGB images, and CSI data. The CSI data is collected from the links between the BS and the users. In all datasets, the users are equipped with a single antenna, while the BS employs either a UPA or ULA configuration,

with adjacent antenna spacing set to half the wavelength at the central frequency. The data is sourced from the dense building scenario in the SynthSoM dataset [28] and the intersection traffic scenario in the M³SC dataset [27]. Note that various communication system configurations are considered, covering a wide range of subcarrier numbers, bandwidths, and antenna sizes. The detailed simulation configurations of the pre-training datasets are presented in Table I.

We also construct a testing set, with detailed simulation configurations shown in Table II. The validation set consists of two parts: 7 test datasets for **seen** scenarios and 3 datasets for **unseen** scenarios. First, to validate the in-distribution performance of WiFo-M², we construct datasets L1 to L7, which are selected from the same links as the pre-training datasets. Among these, datasets L1, L5, and L6 are formed by merging several links with the same number of antennas and subcarriers but smaller data volumes. To test the cross-scenario generalization ability of WiFo-M², we construct datasets C1, S1, and V1 based on three new scenarios not included in the pre-training datasets, namely, the campus scenario in the SynthSoM-Twin dataset [30], the dist_cam scenario in the ViWi dataset [31], and the Scenario 31 in the DeepSense-6G dataset [32], respectively. Notably, these three datasets operate at entirely new carrier frequencies, and their images and LiDAR point clouds exhibit visual appearances and spatial

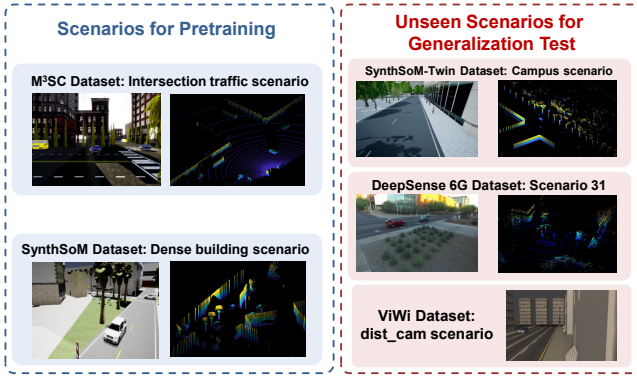


Fig. 5: Overview of multi-modal sensory data from all datasets.

layouts unseen in the pre-training data. This pronounced gap between training and evaluation domains highlights the strong universality and generalization capability of WiFo-M². Fig. 5 provides an overview of the multi-modal data examples from all the aforementioned scenarios.

B. Network and Pre-training Settings

The WiFo-M²-LiDAR is trained for 100 epochs using a batch size of 1024. The optimization employs the AdamW optimizer with a learning rate of 1×10^{-4} and a weight decay of 5×10^{-4} . A cosine annealing learning rate scheduler with a warm-up phase is utilized: the learning rate linearly increases from zero to the target learning rate over the first 10 epochs, then decays following a cosine schedule to zero by the final epoch. The contrastive learning objective is optimized with an initial temperature parameter $\tau_e = 0.1$ and the output feature dimension d set to 512. We set the loss weights in Eq. (16) to $\lambda_1 = 1$, $\lambda_2 = 0.25$, and $\lambda_3 = 0.25$. The WiFo-M²-Img shares the same hyperparameter settings as WiFo-M²-LiDAR, except that the learning rate is set to 5×10^{-4} .

C. Performance Evaluation

The testing dataset introduced in Section V-A is further divided into a training set and a validation set with a ratio of 4 : 1, referred to as the T-T dataset and the T-V dataset, respectively. Note that in all subsequent experiments, the existing schemes are trained on the T-T dataset and their performance is evaluated on the T-V dataset. During this process, the weight of the WiFo-M² model remains **frozen**, and only the existing transceiver design networks and the adapter module are **trained**.

1) Beam Prediction:

- Problem Description: The BP task aims to directly predict the optimal beamforming vector $\mathbf{f}^* \in \mathcal{F}$ from a pre-defined codebook $\mathcal{F} = \{\mathbf{f}_q\}_{q=1}^Q$ at BS using multi-modal sensing. Let $\mathbf{h} \in \mathbb{C}^{1 \times N}$ be the CSI of a certain subcarrier. The optimal vector $\mathbf{f}^* = \arg \max_{m \in \{1, 2, \dots, Q\}} |\mathbf{h}\mathbf{f}_m|^2$ results in the maximum effective channel gain and should be chosen for transmission. The BP task can be formulated as: $\mathbf{f}^* = \mathcal{Q}_{\text{BP}}(\mathbf{M})$, where $\mathcal{Q}_{\text{BP}}(\cdot)$ represents a certain BP scheme and \mathbf{M} is the multi-modal sensory data.

Unlike the other three transceiver design modules, BP entirely relies on multi-modal sensing. Therefore, the WiFo-M² model is directly connected to a 2-layer multilayer perceptron (MLP) network to output the optimal beam index. During fine-tuning on the T-T dataset, only the MLP is trained. Under this setting, the BP performance intuitively reflects the effectiveness of the OOB channel features.

- Existing BP schemes: We selected two existing BP schemes, namely Vision-BP [7] and MM-BP [29]. Vision-BP [7] detects transmitters with the YOLOv3 and then feeds the bounding-box centers to a NN to select the beam index. MM-BP [29] is a multi-modal fusion based scheme that extracts features from images, radar, and LiDAR.
- Experiment Settings: The training hyperparameters for Vision-BP and MM-BP schemes are kept identical to those used in [7] and [29]. The proposed WiFo-M²-based BP scheme is trained with a batch size of 32 and an initial learning rate of 2×10^{-4} , without any learning rate decay.
- WiFo-M²'s Performance: We evaluate the performance of BP task using the top- k accuracy metric. This metric measures the percentage of test samples for which the ground-truth optimal beam is included in the model's k highest-ranked predictions. In our experiments, we report results for $k = 1, 3, 5$ to comprehensively assess the prediction capability.

As shown in Fig. 6, across all 7 datasets, the proposed WiFo-M² models exhibit highly competitive prediction accuracy even though the backbones are completely frozen. The WiFo-M²-Img scheme attains noticeably higher Top-1 prediction accuracy than Vision-BP scheme on L4, L5 and L6, whereas on the remaining four datasets its performance is only slightly lower than that of Vision-BP. This demonstrates that the WiFo-M²-Img backbone acquires channel-aware knowledge extracted during pre-training. The effect is more pronounced on LiDAR-based BP task: WiFo-M²-LiDAR substantially surpasses the fully-trained MM-BP-LiDAR baseline on every dataset, which indicates that the pre-trained WiFo-M²-LiDAR captures spatial patterns that are highly predictive of the optimal beam. When both modalities are available, WiFo-M² delivers virtually the same performance as the MM-BP scheme, with a mean Top-1 gap of only 2%. In summary, the BP results confirm that the Contra-SoM pre-training aligns visual and LiDAR features with the wireless channel domain. Consequently, high-quality beam selection can be achieved with minimal retraining overhead.

2) Channel Estimation:

- Problem Description: CE task refers to the process in which the BS estimates the channel \mathbf{h} at the pilot-placed subcarriers. We assume that the BS adopts the hybrid (analog/digital) structure and is equipped with N_{RF} RF chains. The digital and analog precoding matrix are represented by $\mathbf{F}_B \in \mathbb{C}^{N_{\text{RF}} \times N_{\text{RF}}}$ and $\mathbf{F}_R \in \mathbb{C}^{N \times N_{\text{RF}}}$ with $\|\mathbf{F}_R \mathbf{F}_B\|_F^2 = N_{\text{RF}}$. \mathbf{F}_B is set as an identity matrix $\mathbf{I}_{N_{\text{RF}}}$ during the CE stage. The quantization bit number

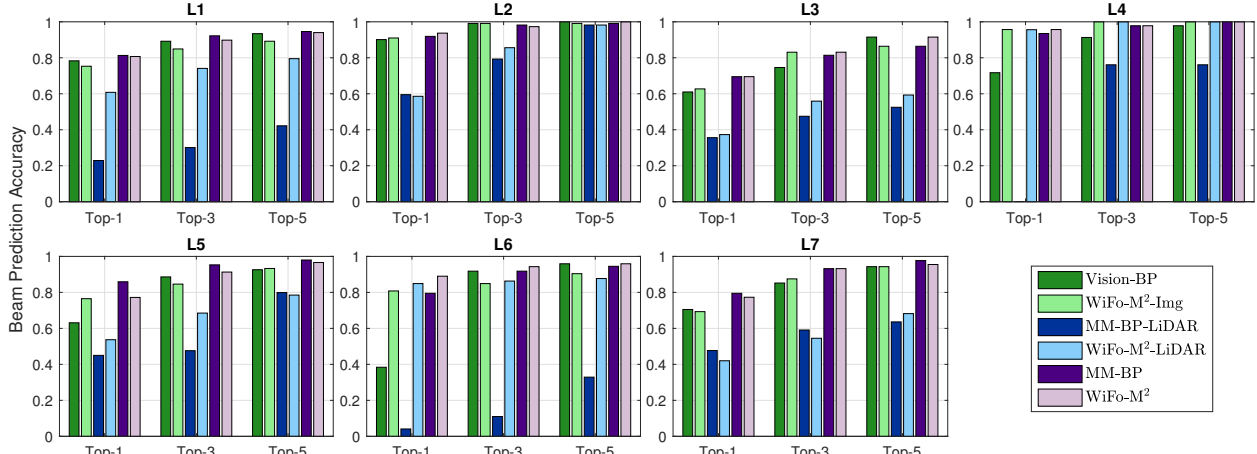


Fig. 6: The Top- k accuracies ($k \in \{1, 3, 5\}$) of the WiFio-M²-based BP scheme, Vision-BP scheme, and MM-BP scheme.

of the phase shifters adopted at BS is set to $B = 3$. Each element of \mathbf{F}_R is randomly chosen from the set $\{e^{\frac{j2\pi n}{Q}}, n = 1, 2, \dots, Q\}$, where $Q \triangleq 2^B = 8$. During the channel estimation stage, the single-antenna user transmits known pilots $\mathbf{x} \in \mathbb{C}^{1 \times T}$ over T successive time slots. The received signal sequence at BS $\mathbf{Y} \in \mathbb{C}^{N_{RF} \times T}$ can then be expressed as:

$$\mathbf{Y} = \mathbf{F}_B^H \mathbf{F}_R^H \mathbf{h}^H \mathbf{x} + \mathbf{F}_B^H \mathbf{F}_R^H \mathbf{n}, \quad (19)$$

where \mathbf{n} denotes the additive white Gaussian noise with i.i.d. entries of zero mean and variance σ^2 . Upon receiving the pilots, BS employs a certain CE network to estimate the CSI: $\hat{\mathbf{h}} = \mathcal{Q}_{CE}(\mathbf{Y}, \mathcal{G}(\mathbf{M}))$, where $\mathcal{Q}_{CE}(\cdot)$ represents a certain CE scheme and $\mathcal{G}(\cdot)$ denotes the WiFio-M² model.

- Existing CE schemes: We selected two existing CE schemes, namely CENN [33] and FCDAMP [34]. CENN [33] predicts the beam-space channel magnitudes and reconstructs the channel from the dominant coefficients, whereas FCDAMP [34] inserts a fully convolutional denoising network into a learned approximate message passing loop to iteratively remove noise and recover the channel.
- Experiment Settings: The number of time slots T is set to 8 for the CENN scheme and 16 for the FCDAMP scheme, while the number of RF chains N_{RF} is 4 for all test datasets and schemes. The learning rate for all schemes is set to 1×10^{-4} , and the batch size is 32.
- WiFio-M²'s Performance: The normalized mean square error (NMSE) is used as the estimation performance metric given by $NMSE = \|\hat{\mathbf{H}} - \mathbf{H}\|_F^2 / \|\mathbf{H}\|_F^2$. We evaluate the channel estimation performance of CENN and FCDAMP schemes under varying SNR conditions. As shown in Fig. 7, the WiFio-M²-enhanced variants consistently outperform the original CENN and FCDAMP models across most datasets and SNRs, demonstrating the general utility of the OOB channel features. Furthermore, the multi-modal fusion (WiFio-M²) typically yields the most robust and significant gains, with LiDAR-only and image-only enhancements providing comparable

improvements in most scenarios. On the L3 dataset with a large 256-antenna array and limited pilots, the performance gains are less pronounced and sometimes irregular. This aligns with the expectation that under extremely sparse measurements and high-resolution array requirements, the coarse prior provided by multi-modal sensing becomes less effective in refining the estimation.

3) Channel Interpolation:

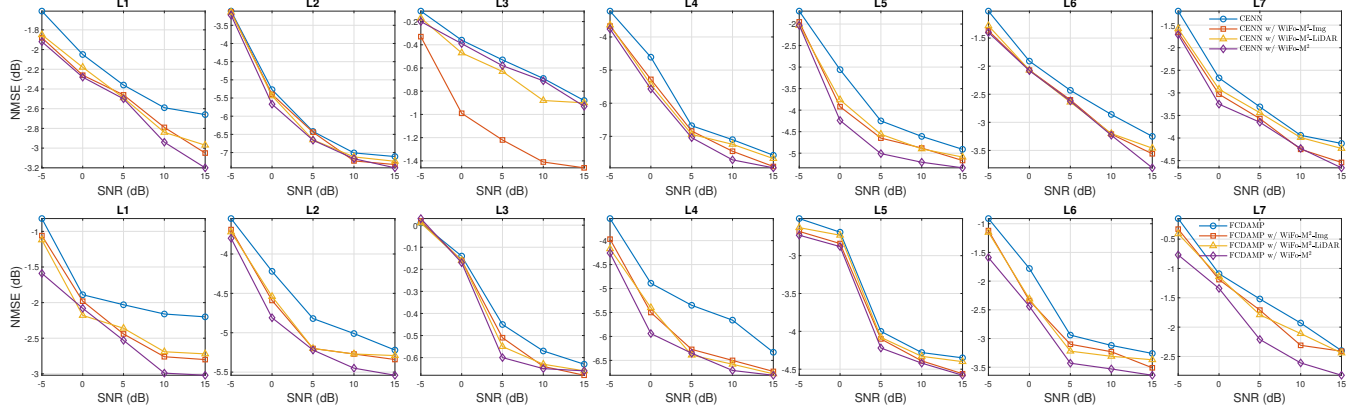
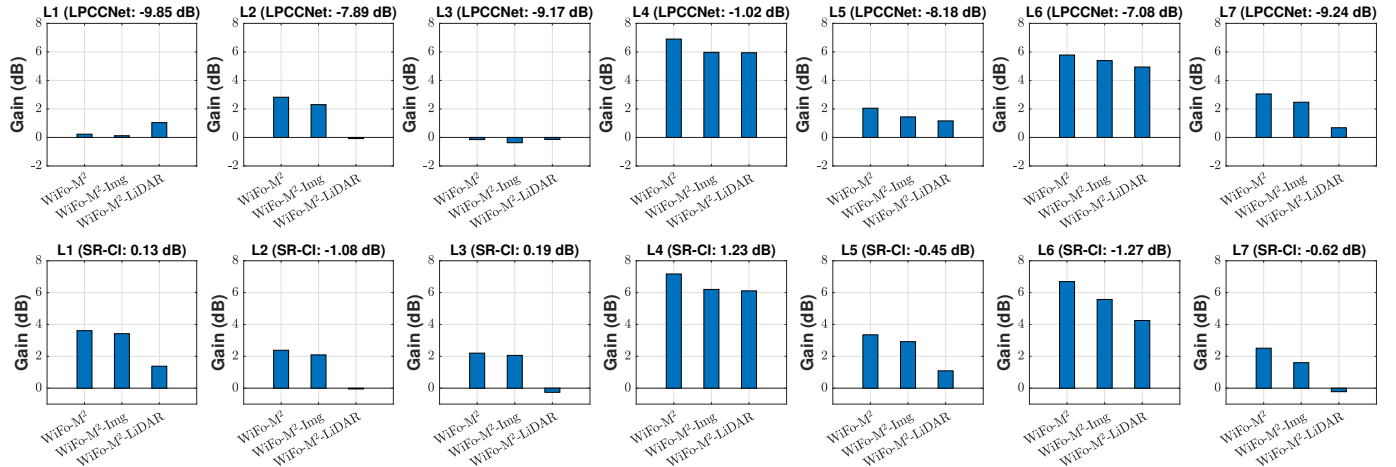
- Problem Description: During the channel estimation stage, pilots are placed only on a subset of subcarriers, and a subset of BS's antenna elements is activated¹. Upon receiving pilots, BS estimates the channel at pilot positions using the Least Squares (LS) algorithm. All the available channel estimates form the low-resolution (LR) channel observation, denoted by $\hat{\mathbf{H}}^{LR} \in \mathbb{C}^{K_p \times N_p}$. Specifically, if pilots are placed every k subcarriers and every x antenna elements, the LR observation can be expressed as:

$$\hat{\mathbf{H}}^{LR}[i, j] = \mathbf{H}[1 : k : K, 1 : x : N] + \mathbf{N}[i, j], \quad (20)$$

where \mathbf{N} denotes the estimation noise. Then, BS utilizes a certain CI scheme to recover the high-resolution (HR) channel image $\hat{\mathbf{H}} \in \mathbb{C}^{K \times N}$. The entire process can be formulated as: $\hat{\mathbf{H}} = \mathcal{Q}_{CI}(\hat{\mathbf{H}}^{LR}, \mathcal{G}(\mathbf{M}))$, where $\mathcal{Q}_{CI}(\cdot)$ represents a certain CI scheme.

- Existing CI schemes: We selected two existing CI schemes, namely SR-CI [36] and LPCCNet [35]. SR-CI [36] obtains a low-precision and low-resolution channel matrix via LS and then feeds the linearly interpolated result into a super-resolution network to enhance the accuracy of CI. LPCCNet [35] is a Laplacian pyramid-based channel completion network that progressively reconstructs the high-resolution channel image from a low-resolution input through a stepwise up-sampling architecture.

¹In our CI task, we assume that a subset of antennas are provided with coarse channel estimates, while the CI schemes are required to recover the full CSI across all antennas. Although this setup does not reflect a practical system configuration, it serves as an effective testbed for evaluating the evaluated CI schemes' ability to perform spatial super-resolution reconstruction.

Fig. 7: CE Performance of CENN and FCDAMP with WiFo-M², WiFo-M²-Img, and WiFo-M²-LiDAR.Fig. 8: Performance gain brought by WiFo-M², WiFo-M²-Img, and WiFo-M²-LiDAR on LPCCNet and SR-CI.

- Experiment Settings: We assume that the pilot placement interval in subcarrier dimension and the sampling ratios for antenna dimensions are set to $k = K/8$ and $x = N/8$, respectively. That is, coarse channel estimates are available on only $1/8$ of the subcarriers and $1/8$ of the antennas, respectively. For network hyperparameters, the SR-CI scheme uses a learning rate of 1×10^{-2} , the LPCCNet scheme uses 1×10^{-4} . The batch size for both schemes is 32.
- WiFo-M²'s Performance: The performance gains of WiFo-M² models over baseline LPCCNet and SR-CI schemes are illustrated in Fig. 8. Among the three variants, WiFo-M² consistently achieves the most stable and significant improvements across different datasets. This demonstrates the effectiveness of multi-modal fusion in enhancing CI accuracy. Note that on the L3 dataset the WiFo-M² models introduce a marginal performance degradation. A likely reason is that the L3 dataset configures a large antenna array, which translates into a very fine angular-resolution requirement for CI. In such a regime, the spatial side information from multi-modal sensing remain too coarse or imperfectly aligned with the complex channel, so the supplementary features cannot improve the high-precision estimates demanded by LPCCNet.

CNet. Moreover, the performance gains brought by WiFo-M² are especially pronounced on the L4 and L6 datasets. L4 employs a BS with a small antenna array, while L6 is configured with relatively fewer subcarriers. Under these reduced spatial- or frequency-resolution settings, the OOB features provided by WiFo-M² are just sufficient to recover the correspondingly lower-dimensional CSI, leading to the sharp performance boost.

4) Channel Prediction:

- Problem Description: In frequency division duplex (FDD) systems, where uplink-downlink reciprocity does not hold, the BS relies on uplink channel feedback to obtain downlink CSI. However, the feedback overhead scales linearly with the number of antennas and devices, making it infeasible for massive MIMO systems. Given that the uplink and downlink transmissions experience the same physical environment, it is reasonable to utilize the uplink CSI measured at the BS to predict the downlink CSI. Similarly to [37], [38], the first half of the subcarriers are considered as the uplink channel, while the remaining half are treated as the downlink channel. Let K_{in} be the number of subcarriers in the first half, and K_{out} represents the number of subcarriers in the second half. Then, the uplink channel \mathbf{H}_d and downlink channel \mathbf{H}_u

TABLE III: CP performance of the WiFo and Transformer-based models, along with their variations enhanced by different WiFo-M² models. The left and right sides of the slash represent the WiFo and Transformer-based schemes, respectively.

Schemes \ Datasets	L1	L2	L3	L4	L5	L6	L7
CP baselines	-5.88/-0.60	-2.41/-0.91	-4.51/-1.38	-0.93/-2.74	-2.36/0	-4.61/-1.15	-2.78/-1.22
CP baselines + WiFo-M ² -Img	-5.84/-0.70	-2.75/0	-5.19/-2.05	-1.15/-3.25	-2.83/1.21	-4.73/-1.13	-3.05/-1.21
CP baselines + WiFo-M ² -LiDAR	-5.92/-0.69	-2.68/ -1.43	-5.07/-1.90	-1.09/-3.12	-3.41/0	-5.04/ -1.32	-2.94/-1.07
CP baselines + WiFo-M ²	-6.02/-0.76	-2.12/-1.12	-5.27/-2.25	-1.27/-3.64	-3.61/0	-5.10/-1.28	-3.30/-1.22

can be expressed as:

$$\mathbf{H}_d = \mathbf{H}[1 : K_{in}, :], \mathbf{H}_u = \mathbf{H}[K_{in} + 1 : K_{in} + K_{out}, :]. \quad (21)$$

The CP task can be formulated as: $\mathbf{H}_u = \mathcal{Q}_{CP}(\mathbf{H}_d, \mathcal{G}(\mathbf{M}))$, where $\mathcal{Q}_{CP}(\cdot)$ represents a certain CP scheme.

- Existing CP schemes: We selected two existing CP schemes, namely WiFo [21] and Transformer-based scheme [39]. WiFo [21] is a wireless FM designed for time/frequency-domain CP, which is pretrained via several self-supervised training tasks. Transformer-based scheme [39] is a parallel CP scheme using Transformer.
- Experiment Settings: The learning rates for the Transformer-based scheme and WiFo are set to 1×10^{-3} and 1×10^{-5} , respectively. The batch size is set to 32. The network input \mathbf{H}_d is assumed to be noisy CSI estimates with an NMSE of -20dB.
- WiFo-M²'s Performance: The performance enhancements provided by WiFo-M² models on top of baseline WiFo and Transformer-based schemes are summarized in Table III. The NMSE is also used as the performance metric. The WiFo-M² model leveraging multi-modality demonstrates its superiority by delivering highest gains for both CP baselines across most datasets, underscoring the benefit of cross-modal feature fusion. Consistent with observations in CI task, performance gains are particularly significant on datasets L4 and L6. Notably, WiFo-M²'s effectiveness is inherently bounded by the convergence of the baseline scheme itself. For instance, on dataset L5, the Transformer-based baseline fails to achieve downlink CSI prediction, and correspondingly, WiFo-M² provides no enhancement. This indicates that the supplementary features cannot compensate for fundamental algorithmic limitations in the baseline model.

D. Ablation Study

In this subsection, we investigate the influence of various specialized designs in both the ContraSoM pre-training strategy and WiFo-M² model, including temporal feature extrapolation (denoted by TFE) and diffusion-based LiDAR feature augmentation (denoted by DA). To highlight the crucial role of the ContraSoM strategy, we additionally evaluate WiFo-M²-Img whose weights are replaced by ImageNet-pre-trained ones, denoted as WiFo-M²-Img w/ INet Weight.

TABLE IV: Results of ablation experiments.

	CE: FCDAMP		CI: LPCCNet		CP: WiFo
WiFo-M ² -Img	-3.38		-9.63		-3.38
WiFo-M ² -Img w/o TFE	-3.23		-8.87		-3.30
WiFo-M ² -Img w/ INet Weight	-3.22		-7.55		-2.96
	CE: FCDAMP		CI: LPCCNet		CP: WiFo
WiFo-M ² -LiDAR	-3.36		-9.13		-3.45
WiFo-M ² -LiDAR w/o DA	-3.27		-8.53		-3.27

Due to page limits, we present ablation results for several representative transceiver design modules, as shown in Table IV. First, removing the temporal feature extrapolation function in WiFo-M² leads to a performance drop, confirming that extrapolating fine-grained future features effectively bridges the sparsity of sensory data. The NMSE results reported are averaged over the L1–L7 datasets. The ablation study results demonstrate the effectiveness of each proposed component. Second, replacing the ContraSoM pretrained weights with generic ImageNet-pretrained weights significantly degrades performance (e.g., from -9.63 to -7.55 on LPCCNet), highlighting the advantage of the supplementary channel features over general-purpose visual features. Third, removing the DA design from WiFo-M²-LiDAR causes a performance decline, validating that the proposed feature-space diffusion process enhances LiDAR representation learning.

E. Cross-Scenario Generalization

In this section, we evaluate the cross-scenario generalization ability of WiFo-M² on the datasets C1, V1, and S1, which are not seen in the pre-training datasets.

1) *S1 Dataset*: The S1 dataset provides measured image and LiDAR point cloud data, as well as the receive power with beams. Due to the absence of CSI, only the performance of the BP task is evaluated on the S1 dataset. The beam prediction task on the S1 dataset is relatively straightforward due to the 16-element antenna array. The Vision-BP baseline achieves Top-1/3/5 accuracies of 91.0%, 98.7%, and 100%, while the MM-BP scheme reaches 92.2%, 100%, and 100%. Notably, the WiFo-M²-img model, with its pre-trained backbone frozen and only a final MLP layer fine-tuned, attains 91.0%, 100%, and 100%, matching or surpassing the strong baselines. This

TABLE V: Evaluation of the enhancement effects of WiFio-M² models on various transceiver design schemes in C1 dataset. Values in bold indicate the best performance.

Schemes	Transceiver Modules		CE: CENN	CE: FCDAMP	CI: LPCCNet	CI: SR-CI	CP: WiFio	CP: Transformer
Baseline			-4.74	-5.30	-16.03	-8.68	-10.74	-14.06
Baseline + WiFio-M ² -Img w/ INet Weight			-4.87	-5.38	-16.73	-7.29	-11.25	-13.58
Baseline + WiFio-M ² -Img w/ ContraSoM Weight			-4.96	-5.43	-17.21	-9.19	-11.58	-14.23
Baseline + WiFio-M ² -LiDAR			-4.77	-5.43	-17.24	-8.59	-11.45	-14.28
Baseline + WiFio-M ²			-4.98	-5.49	-17.29	-9.11	-12.21	-14.26

TABLE VI: Evaluation of the enhancement effects of WiFio-M²-Img model on various transceiver design schemes in V1 dataset. Values in bold indicate the best performance.

Schemes	Transceiver Modules		CE: CENN	CE: FCDAMP	CI: LPCCNet	CI: SR-CI	CP: WiFio	CP: Transformer
Baseline			-3.09	-3.17	-8.81	-3.85	-5.23	-
Baseline + WiFio-M ² -Img w/ INet Weight			-2.33	-4.28	-9.52	-4.32	-5.02	-
Baseline + WiFio-M ² -Img w/ ContraSoM Weight			-3.41	-5.17	-10.46	-4.35	-5.55	-

demonstrates that the representations learned by WiFio-M² successfully generalize to the unseen S1 scenario.

2) *C1 Dataset*: Table V summarizes the cross-scenario generalization performance of WiFio-M² variants when applied to CE, CI, and CP modules on the unseen C1 dataset. As can be seen, the WiFio-M² model with multi-modality provides consistent and often the best performance gains across most schemes, achieving the lowest NMSE for both CE schemes and one CP scheme (WiFio). Importantly, the WiFio-M²-Img consistently outperforms its ImageNet-pre-trained counterpart, confirming the effectiveness of the proposed ContraSoM strategy. BP results exhibit the same trend. Using only LiDAR, the MM-BP-LiDAR baseline achieves top-1/3/5 accuracy of 69.4%, 86.0%, and 86.0%, while WiFio-M²-LiDAR attains 73.1%, 90.3%, and 99.5%. With image alone, the vision-BP baseline delivers 78.5%, 88.2%, and 90.3%, against 77.4%, 85.5%, and 89.2% for WiFio-M²-Img. Under multi-modal fusion, MM-BP scheme peaks at 88.7%, 99.5%, and 100%, whereas WiFio-M² achieves 83.9%, 91.4%, and 93.0%.

3) *V1 Dataset*: The V1 dataset provides only images and CSI data. Hence, we focus on the performance of WiFio-M²-Img. In the BP task, the WiFio-M²-Img-based scheme achieves top-1/3/5 accuracy of 67.4%, 91.2%, and 98.1%, outperforming Vision-BP (65.5%, 82.4%, 92.3%) and closely matching the performance of the MM-BP scheme (71.3%, 87.4%, 99.2%) which uses only its image branch. Table VI presents the enhancement effect of WiFio-M²-Img on other baselines, demonstrating consistent performance improvements across all baselines, with the exception of the Transformer-based CP scheme, which failed to converge. In the same way, the weights derived from the ContraSoM strategy play a significant role.

F. Computational and Deployment Efficiency

To assess the practical deployment overhead of WiFio-M², we evaluate its model complexity and inference latency. All experiments are conducted on a server equipped with dual 14-core Intel Xeon E5-2680 v4 CPUs and an NVIDIA GeForce RTX 4090 GPU, processing inputs with a batch size of 1 to

TABLE VII: Additional fine-tunable parameters introduced by applying WiFio-M² to different transceiver modules.

Transceiver Modules	CE: CENN	CE: FCDAMP	CI: LPCCNet	BP
Parameters (M)	0.13 0.26	0.09 0.18	0.035 0.051	0.067 0.13
Transceiver Modules	CI: SR-CI	CP: WiFio	CP: Transformer	
Parameters (M)	0.017 0.034	0.26 0.26	0.026 0.055	

simulate real-time operation. WiFio-M²-LiDAR comprises only 0.07M parameters with an inference latency of 3.31ms, while WiFio-M²-Img contains 9.62M parameters with an inference latency of 6.04ms. When multiple modalities are available, the total inference can be executed in (at most) the sum of their latencies, i.e., 9.35ms, when processed serially. Even with this upper bound, the system stays well within a real-time budget: at 40 FPS a new multi-modal sample arrives every 25ms, leaving 15.7ms after inference to exploit the freshly produced features. During those 9.35ms, the features predicted from the previous sample can still be used, which only requires the model's output sequence to be extended to cover the 9.35ms inference window

As another practical metric, Table VII presents the additional fine-tunable parameters introduced when WiFio-M² is integrated into various existing transceiver modules. The parameter overhead remains extremely low, reaching at most 0.26M. This is due to the effectiveness and superiority of the ContraSoM pre-training strategy, which allows the WiFio-M² backbone to remain frozen during adaptation and only requires the lightweight adapter to be fine-tuned together with the existing schemes. This further highlights the practical deployability of WiFio-M².

VI. CONCLUSIONS

This paper proposed the first universal foundation model for realizing multi-modal sensing-aided communications, WiFio-

M^2 . To bridge the huge gap between multi-modal sensing and communications, we crafted the ContraSoM pre-training strategy, a contrastive pre-training scheme that leverages diffusion-based augmentation. Empowered by large-scale pre-training, WiFo- M^2 is able to derive fine-grained OOB channel features from sparse historical sensing input, providing a transferable representation that plugs seamlessly into diverse transceiver modules. WiFo- M^2 fundamentally shifts the paradigm from designing isolated, task-specific schemes to flexibly applying the universal representation to optimize existing transceiver design schemes, thereby extending the benefit of multi-modal sensing to a wider range of core transceiver design modules.

REFERENCES

- [1] X. Cheng, D. Duan, S. Gao, and L. Yang, "Integrated Sensing and Communications (ISAC) for Vehicular Communication Networks (VCN)," *IEEE Internet Things J.*, vol. 9, no. 23, pp. 23441–23451, Dec. 2022.
- [2] X. Cheng *et al.*, "Intelligent multi-modal sensing-communication integration: Synesthesia of machines," *IEEE Commun. Surveys Tuts.*, vol. 26, no. 1, pp. 258–301, 1st Quart., 2024.
- [3] H. Zhang, S. Gao, X. Cheng and L. Yang, "Synesthesia of machines (SoM)-enhanced wideband multi-user CSI learning with LiDAR sensing," *IEEE Trans. Veh. Technol.*, vol. 74, no. 8, pp. 13237–13242, Aug. 2025.
- [4] S. Jiang and A. Alkhateeb, "Sensing aided OTFS channel Estimation for Massive MIMO Systems," in *Proc. IEEE Int. Conf. Commun. Workshops (ICC Workshops)*, Rome, Italy, May. 2023, pp. 794–799.
- [5] H. Zhang, S. Gao, X. Cheng and L. Yang, "Integrated sensing and communications toward proactive beamforming in mmWave V2I via multi-modal feature fusion (MMFF)," *IEEE Trans. Wireless Commun.*, vol. 23, no. 11, pp. 15721–15735, Nov. 2024.
- [6] G. Charan, T. Osman, A. Hredzak, N. Thawdar, and A. Alkhateeb, "Vision-position multi-modal beam prediction using real millimeter wave datasets," in *Proc. 2022 IEEE Wireless Commun. Netw. Conf.*, 2022, pp. 2727–2731.
- [7] G. Charan, M. Alrabeiah, T. Osman, and A. Alkhateeb, "Camera based mmWave beam prediction: Towards multi-candidate real-world scenarios," *IEEE Trans. Veh. Technol.*, vol. 74, no. 4, pp. 5897–5913, Apr. 2025.
- [8] H. Zhang, S. Gao, W. Wen, X. Cheng, and L. Yang, "Synesthesia of Machines (SoM)-Aided Online FDD Precoding via Heterogeneous Multi-Modal Sensing: A Vertical Federated Learning Approach," *IEEE Trans. Mobile Comput.*, doi: 10.1109/TMC.2025.3648908, early access.
- [9] B. Salehi, J. Gu, D. Roy, and K. Chowdhury, "FLASH: Federated learning for automated selection of high-band mmWave sectors," in *Proc. IEEE Conf. Comput. Commun. (INFOCOM)*, London, U.K., May. 2022, pp. 1719–1728.
- [10] J. Liang, M. Wen, S. Wang, Y. Liang, and S. Gao, "Aligning Beam with Imbalanced Multi-modality: A Generative Federated Learning Approach," in *Proc. IEEE/CIC Int. Conf. Commun. China (ICCC)*, Shanghai, China, Aug. 2025, pp. 1–6.
- [11] C. Zhou *et al.*, "A comprehensive survey on pretrained foundation models: A history from BERT to ChatGPT," arXiv preprint arXiv:2302.09419, 2023.
- [12] H. Wang *et al.*, "SAM-Med3D: A Vision Foundation Model for General-Purpose Segmentation on Volumetric Medical Images," *IEEE Trans. Neural Netw. Learn. Syst.*, vol. 36, no. 10, pp. 17599–17612, Oct. 2025.
- [13] A. Radford *et al.*, "Learning transferable visual models from natural language supervision," in *Proc. Int. Conf. Mach. Learn. (ICML)*, 2021, pp. 8748–8763.
- [14] Q. Song, J. Hu, L. Xiao, B. Sun, X. Gao and S. Li, "DiffCL: A Diffusion-Based Contrastive Learning Framework With Semantic Alignment for Multimodal Recommendations," *IEEE Trans. Neural Netw. Learn. Syst.*, vol. 36, no. 10, pp. 18587–18597, Oct. 2025.
- [15] L. Liu, A. I. Aviles-Rivero and C. -B. Schönlieb, "Contrastive Registration for Unsupervised Medical Image Segmentation," *IEEE Trans. Neural Netw. Learn. Syst.*, vol. 36, no. 1, pp. 147–159, Jan. 2025.
- [16] N. Wang, P. Feng, Z. Ge, Y. Zhou, B. Zhou and Z. Wang, "Adversarial Spatiotemporal Contrastive Learning for Electrocardiogram Signals," *IEEE Trans. Neural Netw. Learn. Syst.*, vol. 35, no. 10, pp. 13845–13859, Oct. 2024.
- [17] J. Jiang, W. Yu, Y. Li, Y. Gao, and S. Xu, "A MIMO Wireless Channel Foundation Model via CIR-CSI Consistency," arXiv preprint arXiv:2502.11965, 2025.
- [18] G. Pan, H. Chen, S. Zhang, C. Hager, and H. Wymeersch, "Large Wireless Localization Model (LWLM): A Foundation Model for Positioning in 6G Networks", arXiv preprint arXiv:2505.10134, 2025.
- [19] J. Wang, *et al.*, "When Vision-Language Model (VLM) Meets Beam Prediction: A Multimodal Contrastive Learning Framework," arXiv preprint arXiv:2508.00456, 2025.
- [20] M. Farzanullah, H. Zhang, A. B. Sediq, A. Afana, M. Erol-Kantarci, "Wireless Multimodal Foundation Model (WMFM): Integrating Vision and Communication Modalities for 6G ISAC Systems", arXiv preprint arXiv:2512.23897, 2025.
- [21] B. Liu, S. Gao, X. Liu, X. Cheng, and L. Yang, "WiFo: Wireless Foundation Model for Channel Prediction," *Sci. China Inf. Sci.*, vol. 68, no. 1, pp. 1–13, Jun. 2025.
- [22] K. He, X. Zhang, S. Ren, and J. Sun, "Deep residual learning for image recognition," in *Proc. IEEE Conf. Comput. Vis. Pattern Recognit. (CVPR)*, 2016, pp. 770–778.
- [23] C. R. Qi, H. Su, K. Mo, and L. J. Guibas, "PointNet: Deep learning on point sets for 3D classification and segmentation," in *Proc. IEEE Conf. Comput. Vis. Pattern Recognit.*, 2017, pp. 77–85.
- [24] A. Aboah, B. Wang, U. Bagci, and Y. Adu-Gyamfi, "Real-time multi class helmet violation detection using few-shot data sampling technique and YOLOv8," in *Proc. IEEE/CVF Conf. Comput. Vis. Pattern Recognit. Workshops (CVPRW)*, Vancouver, BC, Canada, Jun. 2023, pp. 5349–5357.
- [25] J. Ho, A. Jain, and P. Abbeel, "Denoising diffusion probabilistic models," in *Proc. Int. Conf. Neural Inf. Process. Syst. (NIPS)*, 2020, pp. 6840–6851.
- [26] K. He, H. Fan, Y. Wu, S. Xie, and R. Girshick, "Momentum contrast for unsupervised visual representation learning," in *Proc. IEEE/CVF Conf. Comput. Vis. Pattern Recognit. (CVPR)*, Jun. 2020, pp. 9729–9738.
- [27] X. Cheng *et al.*, "M³SC: A Generic Dataset for Mixed Multi-Modal (MMM) Sensing and Communication Integration," *China Communications*, vol. 20, no. 11, pp. 13–29, Nov. 2023.
- [28] X. Cheng *et al.*, "SynthSoM: A synthetic intelligent multi-modal sensing-communication dataset for Synesthesia of Machines (SoM)," *Sci. Data*, vol. 12, May. 2025.
- [29] B. Shi, M. Li, M.-M. Zhao, M. Lei, and L. Li, "Multimodal deep learning empowered millimeter-wave beam prediction," in *Proc. IEEE 99th Veh. Technol. Conf. (VTC-Spring)*, Singapore, Jun. 2024, pp. 1–6.
- [30] J. Chen, Z. Huang, X. Cai, X. Cheng, and L. Yang, "SynthSoM-Twin: A Multi-Modal Sensing-Communication Digital-Twin Dataset for Sim2Real Transfer via Synesthesia of Machines", arXiv preprint arXiv:2511.11503, 2025.
- [31] M. Alrabeiah, A. Hredzak, Z. Liu, and A. Alkhateeb, "ViWi: A Deep Learning Dataset Framework for Vision-Aided Wireless Communications," in *Proc. IEEE 91st Veh. Technol. Conf. (VTC-Spring)*, Antwerp, Belgium, May. 2020, pp. 1–5.
- [32] A. Alkhateeb *et al.*, "DeepSense 6G: A large-scale real-world multi-modal sensing and communication dataset," *IEEE Commun. Mag.*, vol. 61, no. 9, pp. 122–128, Sep. 2023.
- [33] W. Ma, C. Qi, Z. Zhang, and J. Cheng, "Sparse Channel Estimation and Hybrid Precoding Using Deep Learning for Millimeter Wave Massive MIMO," *IEEE Trans. Commun.*, vol. 68, no. 5, pp. 2838–2849, May. 2020.
- [34] Y. Zhang, Y. Mu, Y. Liu, T. Zhang, and Y. Qian, "Deep learning-based beamspace channel estimation in mmWave massive MIMO systems," *IEEE Wireless Commun. Lett.*, vol. 9, no. 12, pp. 2212–2215, Dec. 2020.
- [35] K. Zu, Y. He, H. Chen, Y. Zheng and M. Haardt, "Deep Learning Super-Resolution-Based Channel Completion for Massive MISO Systems," *IEEE Signal Process. Lett.*, vol. 32, pp. 2254–2258, 2025.
- [36] Y. Wang, H. Lu, and H. Sun, "Channel estimation in IRS-enhanced mmWave system with super-resolution network," *IEEE Commun. Lett.*, vol. 25, no. 8, pp. 2599–2603, Aug. 2021.
- [37] X. Zhao, Z. An, Q. Pan, and L. Yang, "Nerf2: Neural radio-frequency radiance fields," in *Proc. ACM Annu. Int. Conf. Mobile Comput. Netw. (MobiCom)*, 2023, pp. 1–15.
- [38] Z. Liu, G. Singh, C. Xu, and D. Vasisht, "Fire: enabling reciprocity for fdd mimo systems," in *Proc. ACM Annu. Int. Conf. Mobile Comput. Netw. (MobiCom)*, 2021, pp. 628–641.
- [39] H. Jiang, M. Cui, D. W. K. Ng and L. Dai, "Accurate Channel Prediction Based on Transformer: Making Mobility Negligible," *IEEE J. Sel. Areas Commun.*, vol. 40, no. 9, pp. 2717–2732, Sept. 2022.